Research Article Vol. 42, No. 3 / March 2025 / Journal of the Optical Society of America A 315

Journal of the Optical Society of America A

OPTICS, IMAGE SCIENCE, AND VISION

Hybrid meshes for the modeling of optical nanostructures with the surface integral equation method

PARMENION MAVRIKAKIS* AND OLIVIER J. F. MARTIN

Nanophotonics and Metrology Laboratory (NAM), École Polytechnique Fédérale de Lausanne (EPFL), 1015 Lausanne, Switzerland
**parmenion.mavrikakis@epfl.ch*

Received 25 October 2024; revised 20 January 2025; accepted 20 January 2025; posted 22 January 2025; published 21 February 2025

Recently, hybrid metasurfaces built from meta-atoms that combine plasmonic and dielectric materials have emerged thanks to their interesting electromagnetic properties. In this study, we resort to surface integral equations (SIEs) and the method of moments (MoM) to model plasmonic and hybrid nanostructures. A surface meshing approach is used to discretize the equations, and the Poggio–Miller–Chang–Harrington–Wu–Tsai (PMCHWT) formulation is considered. To model experimentally relevant nanostructures efficiently, we combine triangular and quadrilateral elements with Rao–Wilton–Glisson (RWG), rooftop, and hybrid basis functions, while an element-by-element approach is used to coalesce triangular and quadrilateral elements. The accuracy and numerical effort associated with each type of mesh are carefully assessed, using a variety of geometries that include one or more materials. Finally, we observe that hybrid meshes are able to accurately reproduce complex scattering features with a significantly reduced number of unknowns.

https://doi.org/10.1364/JOSAA.546221

1. INTRODUCTION

Over the last few decades, plasmonic nanostructures have been extensively studied for their ability to produce strong field enhancements through the resonant oscillation of free electrons [1,2]. However, these resonances face the following significant challenges: the intrinsic losses in metals, which limit the quality factor [3], and their predominantly electric dipolar nature, which restricts the range of possible electromagnetic responses [4]. To address these issues, researchers have turned to dielectrics, which have modest losses [5–9]. Dielectric nanostructures can support both electric and magnetic resonances, enabling phenomena such as unidirectional scattering [10,11] and Fano resonances [12]. Despite these benefits, dielectrics do not offer the same level of field enhancement as metals, which is a drawback for applications like fluorescence [13] and sensing [14]. To overcome the limitations of both metals and dielectrics, hybrid metal–dielectric nanostructures have emerged as a promising solution [15,16]. These structures aim to combine the low losses of dielectrics with the high field enhancement capabilities of metals. Theoretical predictions suggest that hybrid nanostructures functioning as nanoantennas can achieve high directivity and enhanced radiation [17–19], making them promising candidates for fluorescence enhancement [17,19–21] and refractive index sensing [22,23].

The surface integral equation (SIE) method is a widely used numerical approach for analyzing electromagnetic scattering in metallic, dielectric, and composite metallic–dielectric structures [24–27]. Although SIE formulations are usually restricted to piecewise-homogeneous materials, they are very appealing compared to other methods because they only require surface discretization [28]. SIEs can be divided into Fredholm integral equations of the first and second kinds [29]. In computational electromagnetics, the first-kind (homogeneous) Fredholm integral equations offer high accuracy but suffer from poor convergence in iterative solutions due to their unbounded integral operators, resulting in system matrices with large condition numbers [30]. The most popular formulation of this kind is the Poggio–Miller–Chang–Harrington–Wu–Tsai (PMCHWT) formulation [31–33]. On the other hand, the second-kind (inhomogeneous) Fredholm integral equations typically achieve fast convergence in iterative solutions because of the combination of an identity and compact operators. However, their solutions are generally less accurate, making them less suitable for practical applications [34]. In past years, a significant amount of effort has been dedicated to comparing different formulations in terms of accuracy and convergence [35–40], employing finite elements of different types and orders [41–44] and using various discretization and testing schemes [34,45–49].

Although many works have investigated a wide variety of aspects of the SIE method, only a small amount of research efforts have been conducted on the combination of triangular

and quadrilateral elements [50,51]. While such a hybrid mesh approach has been used for computational analysis in other areas [52–54], the SIE method literature does not provide thorough insights and conclusions regarding the advantages and drawbacks of surface discretization with hybrid meshes in optics.

In this paper, the SIEs for the T-PMCHWT formulation, in which the tangential field components are used, are first presented [55]. The surface discretization is then implemented with triangular, quadrilateral, or a combination of these elements. For triangular and quadrilateral elements, the Rao–Wilton–Glisson (RWG) [56] and rooftop basis functions [57] are considered. In order to solve the SIEs, we apply the method of moments (MoM) and use the Galerkin method. Through many numerical examples, which involve plasmonic and hybrid nanostructures, we demonstrate the main differences between purely triangular, quadrilateral, and hybrid discretization schemes in terms of accuracy and computational time.

2. SURFACE INTEGRAL EQUATIONS

In this section, the T-PMCHWT formulation is first reviewed. Time-harmonic fields with a $e^{-j\omega t}$ time dependence are used throughout.

A. Electromagnetic Problem

Consider a three-region geometry as shown in Fig. 1, where a scatterer consisting of two piecewise homogeneous media is placed in a homogeneous background.

Each domain is described by a constant electric permittivity ε_i and magnetic permeability μ_i. For the electric field $\mathbf{E}_i(\mathbf{r})$ and magnetic field $\mathbf{H}_i(\mathbf{r})$ in each region Ω_i, we can write

$$\nabla \times \nabla \times \mathbf{E}_i(\mathbf{r}) - k_i^2 \mathbf{E}_i(\mathbf{r}) = j\omega\mu_i \mathbf{J}_i(\mathbf{r}) \,, \tag{1}$$

$$\nabla \times \nabla \times \mathbf{H}_i(\mathbf{r}) - k_i^2 \mathbf{H}_i(\mathbf{r}) = \nabla \times \mathbf{J}_i(\mathbf{r}) \,, \tag{2}$$

where ω is the angular frequency, $k_i = \omega\sqrt{\varepsilon_i \mu_i}$ denotes the wavenumber in Ω_i, and $\mathbf{J}_i(\mathbf{r})$ is the volume current distribution in Ω_i. The dyadic Green's tensor is given by the expression

$$\overline{\mathbf{G}}(\mathbf{r}, \mathbf{r}') = \left(\overline{\mathbf{1}} + \frac{\nabla\nabla}{k^2}\right) \frac{e^{jk|\mathbf{r}-\mathbf{r}'|}}{4\pi\,|\mathbf{r}-\mathbf{r}'|}, \tag{3}$$

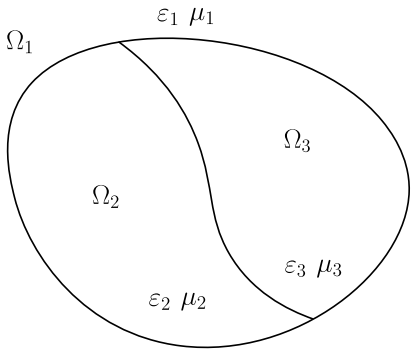

Fig. 1. Geometry of the considered three-region scattering problem.

where $G(\mathbf{r}, \mathbf{r}') = e^{jk|\mathbf{r}-\mathbf{r}'|}/4\pi|\mathbf{r}-\mathbf{r}'|$ is the scalar Green's function in a homogeneous medium with wavenumber k [58]. For the dyadic Green's function $\overline{\mathbf{G}}_i(\mathbf{r}, \mathbf{r}')$ in each domain Ω_i, we can write

$$\nabla \times \nabla \times \overline{\mathbf{G}}_i(\mathbf{r}, \mathbf{r}') - k_i^2 \overline{\mathbf{G}}_i(\mathbf{r}, \mathbf{r}') = \overline{\mathbf{1}}\delta(\mathbf{r}-\mathbf{r}') \,, \tag{4}$$

where we have Kronecker's delta and $\overline{\mathbf{1}}|_{ij} = \delta_{ij}$. By combining Eqs. (1) and (4) and proceeding to a series of calculations that can be found in detail in Ref. [55], we can derive the electric field integral equation (EFIE):

$$\eta_i \mathcal{D}_i\{\mathbf{J}_{s,i}\}(\mathbf{r})\big|_{\tan} + \mathcal{K}_i\{\mathbf{M}_{s,i}\}(\mathbf{r})\big|_{\tan} = \mathbf{E}_i^{\text{inc}}(\mathbf{r})\big|_{\tan}, \tag{5}$$

where $i = 1, 2, 3$, depending on the domain, $\eta_i = \sqrt{\mu_i/\varepsilon_i}$ is the characteristic impedance of the medium in Ω_i, "tan" stands for tangential, $\mathbf{J}_{s,i}(\mathbf{r}) = \hat{\mathbf{n}}_i(\mathbf{r}) \times \mathbf{H}_i(\mathbf{r})$ is the electric surface current density, and $\mathbf{M}_{s,i}(\mathbf{r}) = \mathbf{E}_i(\mathbf{r}) \times \hat{\mathbf{n}}_i(\mathbf{r})$ is the magnetic surface current density defined on the boundary $\partial\Omega_i$ of domain Ω_i. Obviously, both surface current densities satisfy boundary conditions [e.g., $\mathbf{J}_{s,1}(\mathbf{r}) = -\mathbf{J}_{s,2}(\mathbf{r})$ and $\mathbf{M}_{s,1}(\mathbf{r}) = -\mathbf{M}_{s,2}(\mathbf{r})$ on the interface between Ω_1 and Ω_2, since $\hat{\mathbf{n}}_1(\mathbf{r}) = -\hat{\mathbf{n}}_2(\mathbf{r})$ and the tangential field components are continuous across the interface]. The linear integral operators $\mathcal{D}_i\{\mathcal{X}\}(\mathbf{r})$ and $\mathcal{K}_i\{\mathcal{X}\}(\mathbf{r})$ are defined as follows:

$$\mathcal{D}_i\{\mathcal{X}\}(\mathbf{r}) = jk_i \int_{\partial\Omega_i} \mathrm{d}S' \overline{\mathbf{G}}_i(\mathbf{r}, \mathbf{r}') \cdot \mathcal{X}(\mathbf{r}') \,, \tag{6}$$

$$\mathcal{K}_i\{\mathcal{X}\}(\mathbf{r}) = \int_{\partial\Omega_i} \mathrm{d}S' \left[\nabla' \times \overline{\mathbf{G}}_i(\mathbf{r}, \mathbf{r}')\right] \cdot \mathcal{X}(\mathbf{r}') \,. \tag{7}$$

Analogously, the magnetic field integral equation (MFIE) is given by

$$\frac{1}{\eta_i} \mathcal{D}_i\{\mathbf{M}_{s,i}\}(\mathbf{r})\big|_{\tan} - \mathcal{K}_i\{\mathbf{J}_{s,i}\}(\mathbf{r})\big|_{\tan} = \mathbf{H}_i^{\text{inc}}(\mathbf{r})\big|_{\tan}. \tag{8}$$

For the rest of the paper, we consider that incident light exists only in the background medium (domain Ω_1); thus, $\mathbf{E}_2^{\text{inc}}(\mathbf{r}) = \mathbf{H}_2^{\text{inc}}(\mathbf{r}) = \mathbf{E}_3^{\text{inc}}(\mathbf{r}) = \mathbf{H}_3^{\text{inc}}(\mathbf{r}) = \mathbf{0}$.

B. Discretization

In this section, we describe a general discretization scheme for SIEs, which will be implemented with specific mesh elements and functions in the following sections. The discretization process of an integral equation involves two steps. First, the unknown surface current densities in Eqs. (5) and (8) need to be expanded with a set of basis functions as follows:

$$\mathbf{J}_{s,i}(\mathbf{r}) = \sum_{n=1}^{N_e} \alpha_{n,i} \mathbf{f}_{n,i}(\mathbf{r}) \,, \tag{9}$$

$$\mathbf{M}_{s,i}(\mathbf{r}) = \sum_{n=1}^{N_e} \beta_{n,i} \mathbf{f}_{n,i}(\mathbf{r}) \,, \tag{10}$$

where N_e is the number of mesh edges, $\mathbf{f}_{n,i}(\mathbf{r})$ represents the basis functions, and $\alpha_{n,i}$, $\beta_{n,i}$ are the expansion coefficients to be determined (they are initially different for each domain Ω_i).

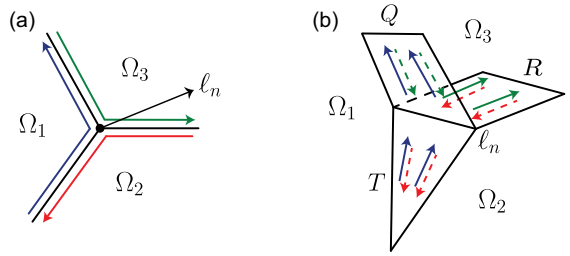

Fig. 2. Graphical representation of a junction ℓ_n bordering three domains. (a) Overview of the basis functions' support in each domain, and (b) basis functions of quadrilateral, triangular, and rectangular elements with ℓ_n as their common junction.

The tangential components of the electric and magnetic fields are continuous across and along a boundary between adjacent domains; thus, the basis functions should be capable of accurately representing a continuous field distribution. For the realization of the latter, we establish the set of basis functions by following an element-by-element approach. Initially, local basis functions are defined separately inside each mesh element, in such a way that boundary conditions between its adjacent regions are fulfilled by default [e.g., $\mathbf{J}_{s,2}(\mathbf{r}) = -\mathbf{J}_{s,3}(\mathbf{r})$ on an element between Ω_2 and Ω_3], and flux density normal to the reference edge of each function is unity. Hence, the desired field continuity across and along the interfaces is fulfilled if all the mesh elements bordering an edge (two adjacent domains) or a junction (edge between multiple adjacent domains, as in Fig. 2) are associated with the same expansion coefficients [24,59]. The procedure regarding the proper function definition inside each element is discussed in Section 3. Consequently, the final set of basis functions can be introduced by combining all the local basis functions $\mathbf{f}^{\text{loc}}_{k,i}(\mathbf{r})$ that border an edge or junction ℓ_n into a single function, as follows:

$$\mathbf{f}_{n,i}(\mathbf{r}) = \sum_{\{k:\ell_k=\ell_n\}} \mathbf{f}^{\text{loc}}_{k,i}(\mathbf{r}) \,, \tag{11}$$

where $\mathbf{f}_{n,i}(\mathbf{r})$ refers to an edge or junction, and ℓ_n and $\mathbf{f}^{\text{loc}}_{k,i}(\mathbf{r})$ refer to an element's local basis function that borders $\ell_k \equiv \ell_n$.

Since $\mathbf{f}^{\text{loc}}_{k,i}(\mathbf{r}) = 0$ if the element does not belong to $\partial\Omega_i$, for the support of the basis function, we have $\text{supp}(\mathbf{f}_{n,i}) \in \partial\Omega_i$. Thus, if ℓ_n borders three domains as in Fig. 2(a), both the sign and the support of $\mathbf{f}_{n,i}(\mathbf{r})$ change with the domain, as shown in Fig. 2(b). Finally, the expansion of the surface current densities can be rewritten as

$$\mathbf{J}_{s,i}(\mathbf{r}) = \sum_{n=1}^{N_e} \alpha_n \mathbf{f}_{n,i}(\mathbf{r}) \,, \tag{12}$$

$$\mathbf{M}_{s,i}(\mathbf{r}) = \sum_{n=1}^{N_e} \beta_n \mathbf{f}_{n,i}(\mathbf{r}) \,, \tag{13}$$

where each edge ℓ_n has a unique set of expansion coefficients and a corresponding basis function. This element-by-element method will be very helpful for the combination of different kinds of elements and functions in a hybrid mesh since the starting point of the procedure is the individual treatment of each element (triangular or quadrilateral).

Second, the integral equations are converted into a matrix system with the aid of a set of testing functions. In the rest of this paper, the Galerkin testing procedure is applied [60], which means that the sets of testing and basis functions coincide. Thus, the EFIE and MFIE become, respectively,

$$[\eta_i \mathbf{D}_i \quad \mathbf{K}_i] \cdot \begin{bmatrix} \boldsymbol{\alpha} \\ \boldsymbol{\beta} \end{bmatrix} = \mathbf{R}^E_i, \tag{14}$$

$$\begin{bmatrix} -\mathbf{K}_i & \eta_i^{-1}\mathbf{D}_i \end{bmatrix} \cdot \begin{bmatrix} \boldsymbol{\alpha} \\ \boldsymbol{\beta} \end{bmatrix} = \mathbf{R}^H_i, \tag{15}$$

where $\mathbf{D}_i$, $\mathbf{K}_i$ are $N_e \times N_e$ square matrices, $\boldsymbol{\alpha}$ and $\boldsymbol{\beta}$ are the column vectors that contain the expansion coefficients, and $\mathbf{R}^E_i$, $\mathbf{R}^H_i$ are the electric and magnetic incident field excitation column vectors. The elements of the previously mentioned quantities are defined as follows:

$$(D_i)_{\text{mn}} = \int_{\partial\Omega_i} \text{d}S \mathbf{f}_{m,i}(\mathbf{r}) \cdot \int_{\partial\Omega_i} \text{d}S' \overline{\mathbf{G}}_i(\mathbf{r}, \mathbf{r}') \cdot \mathbf{f}_{n,i}(\mathbf{r}') \,, \tag{16}$$

$$(K_i)_{mn} = \int_{\partial\Omega_i} \text{d}S \mathbf{f}_{m,i}(\mathbf{r}) \int_{\partial\Omega_i} \text{d}S' \left[\nabla' \times \overline{\mathbf{G}}_i(\mathbf{r}, \mathbf{r}')\right] \cdot \mathbf{f}_{n,i}(\mathbf{r}') \,, \tag{17}$$

$$\left(R^E_i\right)_m = \int_{\partial\Omega_i} \text{d}S \mathbf{f}_{m,i}(\mathbf{r}) \cdot \mathbf{E}^{\text{inc}}_i(\mathbf{r}) \,, \tag{18}$$

$$\left(R^H_i\right)_m = \int_{\partial\Omega_i} \text{d}S \mathbf{f}_{m,i}(\mathbf{r}) \cdot \mathbf{H}^{\text{inc}}_i(\mathbf{r}) \,, \tag{19}$$

$$\alpha = [\alpha_1 \quad \ldots \quad \alpha_{N_e}]^T, \tag{20}$$

$$\beta = [\beta_1 \quad \ldots \quad \beta_{N_e}]^T. \tag{21}$$

The EFIE and MFIE formulations lack unique solutions at certain frequencies, specifically at the resonant frequencies of the cavity formed by the surface $\partial\Omega_i$ of a perfect electric conductor (PEC) filled with the material from the exterior region of the original problem [61]. This issue can be addressed by appropriately combining the EFIE and MFIE equations. One combination that provides accurate solutions even under resonant conditions is the T-PMCHWT formulation. In this approach, the EFIEs for all domains are summed together, as are the MFIEs, and these combined equations are then solved simultaneously. Hence, the final matrix system has the following form:

$$\sum_i \begin{bmatrix} \eta_i \mathbf{D}_i & \mathbf{K}_i \\ -\mathbf{K}_i & \eta_i^{-1}\mathbf{D}_i \end{bmatrix} \cdot \begin{bmatrix} \boldsymbol{\alpha} \\ \boldsymbol{\beta} \end{bmatrix} = \sum_i \begin{bmatrix} \mathbf{R}^E_i \\ \mathbf{R}^H_i \end{bmatrix}. \tag{22}$$

This method can be applied to electromagnetic scattering problems with an arbitrary number of domains.

3. ELEMENTS AND BASIS FUNCTIONS

A comparison of the solution accuracy and simulation time requires the implementation of homogeneous (only triangular or quadrilateral mesh elements) and hybrid (triangular and quadrilateral mesh elements) discretization schemes, which

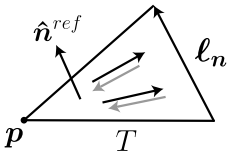

Fig. 3. Half-RWG (hRWG) function.

Table 1. Half-RWG and Half-Rooftop Functions' Signs

Direction of $\hat{\mathbf{n}}^{\text{ref}}$	$s > 0$	$s < 0$
Toward the interior of Ω_i	+	−
Toward the exterior of Ω_i	−	+

will be described in this section. In general, the basis and testing functions can be categorized into divergence-conforming [62] and curl-conforming functions [63]. Since the basis functions have to model the unknown electric and magnetic surface current densities, they should be divergence-conforming in order to properly model the electric ($\rho_{s,e} = \nabla \cdot \mathbf{J}_s$) and magnetic ($\rho_{s,m} = \nabla \cdot \mathbf{M}_s$) surface charge densities and the currents' continuity. In this paper, because of their versatility, we choose the RWG and the rooftop functions as the basis for triangular and quadrilateral elements, respectively.

A. Triangular Discretization

In computational electromagnetics, the most popular elements for surface discretization are triangles. Triangular elements are very convenient because they can model complex geometrical details better than other kinds of elements. For a triangular mesh of a given surface, we resort to the modified half-RWG (hRWG) basis function [56], which is applied in a single triangle, as shown in Fig. 3. Each edge in the triangular mesh has a specific direction that is chosen arbitrarily, which means that every edge is characterized by a fixed vector $\boldsymbol{\ell}_n$ and its length ℓ_n. Hence, for a mesh triangle T with surface area A and a vertex $\mathbf{p}$ (opposite to ℓ_n), the corresponding hRWG function is defined as

$$\mathbf{f}_{n,i}^{\text{hRWG}}(\mathbf{r}) = \begin{cases} \pm\frac{\ell_n}{2A}(\mathbf{r}-\mathbf{p}), & \mathbf{r} \in T \\ 0, & \mathbf{r} \notin T \end{cases}, \tag{23}$$

where $\mathbf{r}$ is the position vector.

The reference normal unit vector $\hat{\mathbf{n}}^{\text{ref}}$ points toward the direction defined by the counterclockwise rotation of the triangle's vertices (they are initially defined for each triangle once). Hence, the reference unit vector is constant in every triangular element and independent of which domain is being considered. For each domain Ω_i, the sign of $\mathbf{f}_{n,i}^{\text{hRWG}}(\mathbf{r})$ is determined by Table 1, where

$$s = \left(\boldsymbol{\ell}_n \times \hat{\mathbf{n}}^{\text{ref}}\right) \cdot (\mathbf{r}-\mathbf{p}), \quad \mathbf{r} \in T \,\&\, \mathbf{r} \neq \mathbf{p}. \tag{24}$$

According to Table 1, it is evident that for two adjacent domains, the hRWG functions have opposite signs [e.g., $\mathbf{f}_{n,1}^{\text{hRWG}}(\mathbf{r}) = -\mathbf{f}_{n,2}^{\text{hRWG}}(\mathbf{r})$ for an edge ℓ_n between Ω_1 and Ω_2 in Fig. 1]. Consequently, the boundary conditions for the surface current densities are satisfied. Finally, by simply combining both hRWG functions that border an edge ℓ_n into a single RWG function, as shown in Fig. 4, we have the expression

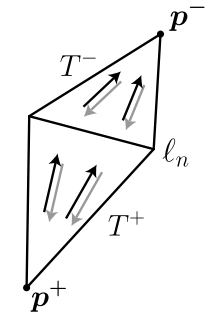

Fig. 4. RWG function.

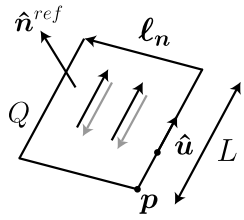

Fig. 5. Half-rooftop function.

$$\mathbf{f}_{n,i}^{\text{RWG}}(\mathbf{r}) = \begin{cases} \pm\frac{\ell_n}{2A^+}(\mathbf{r}-\mathbf{p}^+), & \mathbf{r} \in T^+ \\ \mp\frac{\ell_n}{2A^-}(\mathbf{r}-\mathbf{p}^-), & \mathbf{r} \in T^- \\ 0, & \text{otherwise} \end{cases}, \tag{25}$$

where A^+, A^- and $\mathbf{p}^+$, $\mathbf{p}^-$ are the surface areas and vertices opposite to the common edge ℓ_n of triangles T^+ and T^-, respectively. Since we associate each edge ℓ_n with one pair of expansion coefficients α_n, β_n, regardless of which bordering triangles and which domain we examine, proper continuity of the surface currents is insured.

B. Quadrilateral Discretization

Another type of discretization element is the quadrilateral. In order to examine quadrilaterals, we first study a special case of this element category, the rectangular element.

1. Planar Rectangular Elements

On a single rectangle, we employ the modified half-rooftop (hRf) basis function [57], as shown in Fig. 5. Similarly to hRWG, each edge has a specific direction $\boldsymbol{\ell}_n$ and length ℓ_n. Thus, in a rectangular element Q, a hRf function is defined as

$$\mathbf{f}_{n,i}^{\text{hRf}}(\mathbf{r}) = \begin{cases} \pm\frac{(\mathbf{r}-\mathbf{p})\cdot\hat{\mathbf{u}}}{L}\hat{\mathbf{u}}, & \mathbf{r} \in Q \\ 0, & \mathbf{r} \notin Q \end{cases}, \tag{26}$$

where L is the length of the edge that is perpendicular to ℓ_n, and $\hat{\mathbf{u}}$ is the normal unit vector of the aforementioned edge with direction from $\mathbf{p}$ toward the next vertex of Q, according to the counterclockwise order of the element's vertices.

Concerning the reference normal unit vector $\hat{\mathbf{n}}^{\text{ref}}$ and the sign determination of the hRf function, the same approach as with hRWG is followed. The only difference is that we consider a different s parameter:

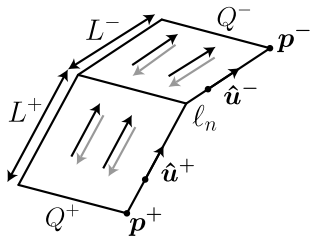

Fig. 6. Rooftop function.

$$s = \left(\boldsymbol{\ell}_n \times \hat{\mathbf{n}}^{\text{ref}}\right) \cdot \hat{\mathbf{u}}. \tag{27}$$

Hence, on the boundary between two adjacent regions, the hRf basis function satisfies the boundary conditions, as was discussed in Section 2.B. Moreover, by assembling the hRf functions in the same way as was done for hRWG, the rooftop function (Rf), as shown in Fig. 6, can be written as

$$\mathbf{f}_{n,i}^{Rf}(\mathbf{r}) = \begin{cases} \pm\frac{(\mathbf{r}-\mathbf{p}^+)\cdot\hat{\mathbf{u}}^+}{L^+}\hat{\mathbf{u}}^+, & \mathbf{r}\in Q^+ \\ \mp\frac{(\mathbf{r}-\mathbf{p}^-)\cdot\hat{\mathbf{u}}^-}{L^-}\hat{\mathbf{u}}^-, & \mathbf{r}\in Q^- \\ 0, & \text{otherwise} \end{cases}, \tag{28}$$

where L^+, L^- are the lengths of the edges that are perpendicular to ℓ_n, $\mathbf{p}^+$ and $\mathbf{p}^-$ are the vertices opposite to the common edge ℓ_n, and $\hat{\mathbf{u}}^+$, $\hat{\mathbf{u}}^-$ are the normal unit vectors of the aforementioned vertical edges, as illustrated in Fig. 6. Similarly to RWG, a unique set of expansion coefficients is used for ℓ_n; thus, the bordering rectangles and considered domain do not affect the continuity of the surface current densities, which is guaranteed.

2. Planar Arbitrary Elements

To develop arbitrary quadrilateral elements, we first introduce a rectangular parametric space (ξ, η), where $\xi \in [0, 1]$ and $\eta \in [0, 1]$, in order to transform the original arbitrary quadrilateral into the unit square. This mapping is depicted clearly in Fig. 7, where the numbers inside the parentheses (in the unit square of the rectangular domain) denote the vertices of the initial quadrilateral element after the application of the transformation. The following analysis is focused on arbitrary planar quadrilaterals with basis functions that are derived from the rooftop function (defined in the parametric space), but a similar approach can be considered for curvilinear quadrilaterals or for higher-order basis functions [57,64,65]. The representation provided in Fig. 7 can be described by the relation

$$\begin{aligned}\mathbf{r} &= \mathbf{r}(\xi, \eta) \\ &= \mathbf{r}_0(1-\xi)(1-\eta) + \mathbf{r}_1\xi(1-\eta) + \mathbf{r}_2\xi\eta + \mathbf{r}_3(1-\xi)\eta.\end{aligned} \tag{29}$$

In this manner, for the surface area and the normal unit vector of the element, we have

$$\mathrm{d}S = \left|\mathbf{r}_\xi \times \mathbf{r}_\eta\right| \mathrm{d}\xi\,\mathrm{d}\eta, \tag{30}$$

$$\hat{\mathbf{n}} = \frac{\mathbf{r}_\xi \times \mathbf{r}_\eta}{\left|\mathbf{r}_\xi \times \mathbf{r}_\eta\right|}. \tag{31}$$

Thus, the corresponding Jacobian is

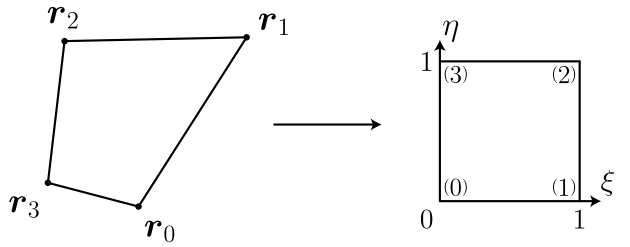

Fig. 7. Mapping an arbitrary quadrilateral element into the parametric unit square in the (ξ, η) domain.

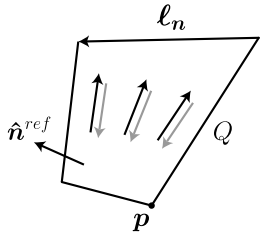

Fig. 8. Half-basis function on the original quadrilateral element.

$$J(\xi, \eta) = \left|\mathbf{r}_\xi \times \mathbf{r}_\eta\right|, \tag{32}$$

where the covariant vectors $\mathbf{r}_\xi$ and $\mathbf{r}_\eta$ are the following:

$$\mathbf{r}_\xi = \frac{\partial \mathbf{r}(\xi, \eta)}{\partial \xi} = (1-\eta)(\mathbf{r}_1 - \mathbf{r}_0) + \eta(\mathbf{r}_2 - \mathbf{r}_3), \tag{33}$$

$$\mathbf{r}_\eta = \frac{\partial \mathbf{r}(\xi, \eta)}{\partial \eta} = (1-\xi)(\mathbf{r}_3 - \mathbf{r}_0) + \xi(\mathbf{r}_2 - \mathbf{r}_1). \tag{34}$$

Finally, we can formulate appropriate relations inside the unit square of the parametric domain that describe the half-basis function in the original quadrilateral element (as shown in Fig. 8). Since the relations are defined in the parametric domain, each one of the element's four half-basis functions has a unique equation, which can be written as

$$\mathbf{f}_{n,i}^{hQ}(\mathbf{r}) \begin{cases} \pm\frac{\xi}{\left|\mathbf{r}_\xi\times\mathbf{r}_\eta\right|}\mathbf{r}_\xi, & \mathbf{r}\in Q, \quad \mathbf{p}=\mathbf{r}_0 \\ \pm\frac{\eta}{\left|\mathbf{r}_\xi\times\mathbf{r}_\eta\right|}\mathbf{r}_\eta, & \mathbf{r}\in Q, \quad \mathbf{p}=\mathbf{r}_1 \\ \mp\frac{1-\xi}{\left|\mathbf{r}_\xi\times\mathbf{r}_\eta\right|}\mathbf{r}_\xi, & \mathbf{r}\in Q, \quad \mathbf{p}=\mathbf{r}_2 \\ \mp\frac{1-\eta}{\left|\mathbf{r}_\xi\times\mathbf{r}_\eta\right|}\mathbf{r}_\eta, & \mathbf{r}\in Q, \quad \mathbf{p}=\mathbf{r}_3 \\ 0, & \text{otherwise} \end{cases}. \tag{35}$$

The basis function for a pair of arbitrary planar quadrilateral elements is presented in Fig. 9; it is built in the same way as the RWG and the Rf basis functions for triangular and rectangular elements, respectively (see Sections 3.A and 3.B.1).

C. Hybrid Discretization

A hybrid mesh that combines different kinds of elements for the discretization of surface boundaries can be advantageous for specific scattering problems. In this paper, we employ a combination of planar triangular and quadrilateral (or rectangular) elements; thus, two adjacent elements can have the same or different geometries. In Sections 3.A and 3.B, we analyzed the former case, whereas the latter is presented in this section. As

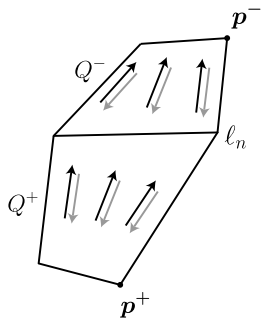

Fig. 9. Basis function on the original pair of quadrilateral elements.

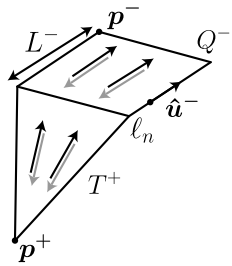

Fig. 10. Hybrid basis function for triangular and rectangular adjacent elements.

mentioned in Section 2.B, our hybrid mesh implementation follows an element-by-element logic, which lets us examine every triangle or quadrilateral independently. Hence, a simple combination of the half-basis functions of neighboring elements, with different geometry types, into a hybrid basis function is straightforward.

In Fig. 10, the case of a triangle–rectangle (TR) combination is illustrated, where the hybrid basis function has the form

$$\mathbf{f}_{n,i}^{\mathrm{TR}}(\mathbf{r}) = \begin{cases} \pm\frac{\ell_n}{2A^+}\left(\mathbf{r}-\mathbf{p}^+\right), & \mathbf{r}\in T^+ \\ \mp\frac{(\mathbf{r}-\mathbf{p}^-)\cdot\hat{\mathbf{u}}^-}{L^-}\hat{\mathbf{u}}^-, & \mathbf{r}\in Q^- \\ 0, & \text{otherwise} \end{cases}. \tag{36}$$

Analogously, for the scenario in Fig. 11, where the rectangular element is replaced by an arbitrary planar quadrilateral (TQ: triangle–quadrilateral case), the basis function can be expressed as

$$\mathbf{f}_{n,i}^{\mathrm{TQ}}(\mathbf{r}) = \begin{cases} \pm\frac{\ell_n}{2A^+}\left(\mathbf{r}-\mathbf{p}^+\right), & \mathbf{r}\in T^+ \\ \mathbf{f}_{n,i}^{hQ}(\mathbf{r}), & \mathbf{r}\in Q^- \\ 0, & \text{otherwise} \end{cases}, \tag{37}$$

where $\mathbf{f}_{n,i}^{hQ}(\mathbf{r})$ is defined in the rectangular parametric space, as in Eq. (35). A very important detail is that all the basis functions (including hybrid ones) have to remain divergence-conforming; thus, they must maintain first-order normal-vector continuity across the common edge ℓ_n [62]. Consequently, one should be extremely careful while implementing the functions and all the calculations that lead to the final linear system of equations.

4. NUMERICAL RESULTS

This section presents various examples that confirm the validity of the hybrid approach and demonstrate the performance

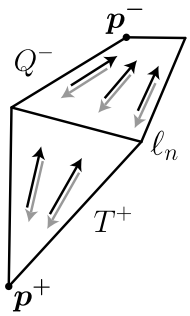

Fig. 11. Hybrid basis function for triangular and quadrilateral adjacent elements.

differences between purely triangular–quadrilateral and hybrid meshes from different computational perspectives. For all the following results, we excite the scattering body with an incident plane wave that is propagating toward the z direction and is polarized along the x axis. To validate our results, we resort in Section 4.A to Mie theory [66], whereas for the following sections, we employ the SIE method as implemented in Refs. [55,67]. The complex values of electric permittivity ε for silver (Ag) and amorphous silicon (aSi) are taken from Refs. [68,69], respectively.

A. Silver Sphere

At first, we validate the correct implementation of the element-by-element approach, and we proceed with a comparison between the accuracy of homogeneous triangular or quadrilateral meshes as the discretization becomes denser and the degrees of freedom (DoF) increase.

First, we consider the analytical solution for the scattering cross section (SCS) of a spherical silver nanoparticle with a radius of $R = 75$ nm, as shown in Fig. 12. Afterward, we discretize the spherical surface of the nanoparticle with a triangular or a quadrilateral mesh, which is gradually refined until it reaches a number of approximately 20,000 DoF (Fig. 13). Finally, we demonstrate the accuracy of the two different mesh types, by presenting the SCS convergence at the wavelength $\lambda = 368$ nm, as well as the average relative error over the whole spectrum, which is defined as

$$R_E = \left(\sum_{\lambda}\frac{\left|\mathrm{SCS}_\lambda - \mathrm{SCS}_{\mathrm{ref},\lambda}\right|}{\mathrm{SCS}_{\mathrm{ref},\lambda}}\right)/\Lambda, \tag{38}$$

where SCS_λ is the numerical value of the scattering cross section at wavelength λ, $\mathrm{SCS}_{\mathrm{ref},\lambda}$ is the corresponding analytical value from the Mie solution, and Λ is the number of the different wavelengths that were considered in the spectrum ($\Lambda = 101$ since we scan with a step of 2 nm). Regarding Green's function, we select the points of numerical integration very carefully so that we avoid the occurrence of singularities. The singularity subtraction method, as implemented in Ref. [70], will be employed in Section 4.C for a hybrid triangular–rectangular mesh. For the spherical and the following cubic geometries, we do not apply singularity subtraction because the meshes are not very dense, and we use a small number of integration points per element. However, we acknowledge that neglecting

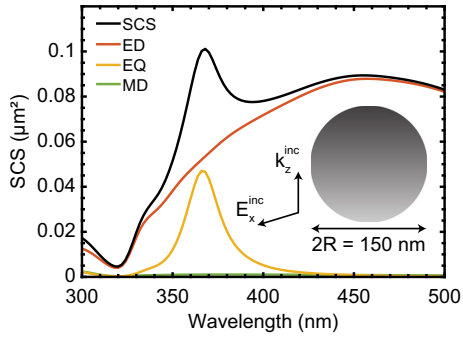

Fig. 12. SCS for a silver sphere ($R = 75$ nm) obtained from the Mie theory.

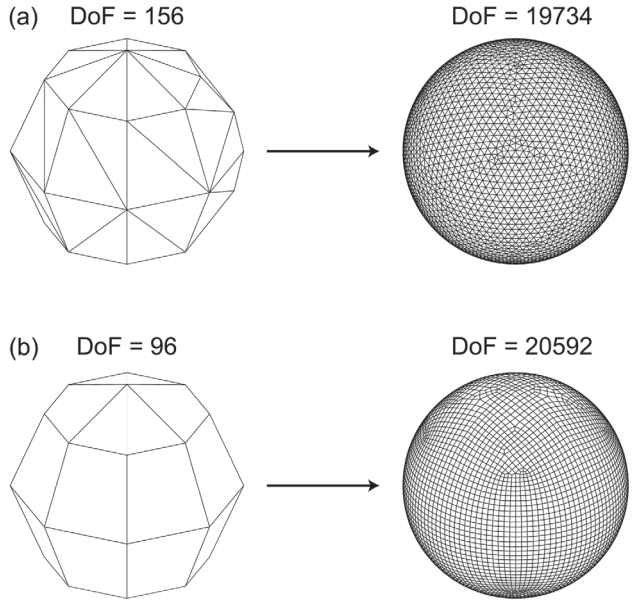

Fig. 13. Initial and final discretization stages for the sphere mesh refinement, using (a) a triangular mesh and (b) a quadrilateral mesh.

a semi-analytical treatment of the static part of the Green's function may introduce inaccuracies in much denser meshes or when employing a higher number of integration points. In such cases, singularity subtraction or cancellation techniques would be necessary to maintain accuracy.

According to the results shown in Fig. 14, both discretization approaches function properly and provide correct scattering responses, even though no more than four numerical integration points were used in each element. Furthermore, the quadrilateral mesh presents a slightly lower relative error in both cases (at resonant wavelength and over the total spectrum) as the number of DoF increases. Although there is an exception at 1260 DoF, in general, the convergence rate is similar for both meshes.

B. Silver Cube with Sharp Edges

In this section, we discretize a silver cube with a side $D = 75$ nm and investigate the performances of triangular and rectangular meshes on this geometry. The reference SCS (Fig. 15) is obtained with the triangular discretization in Fig. 16, with

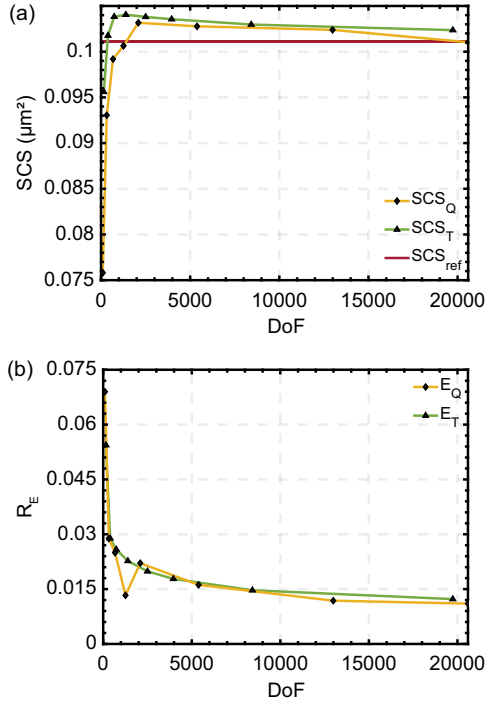

Fig. 14. Accuracy and convergence comparisons between triangular and quadrilateral meshes. (a) SCS accuracy at the resonance $\lambda = 368$ nm, and (b) convergence of the relative error over the entire spectrum.

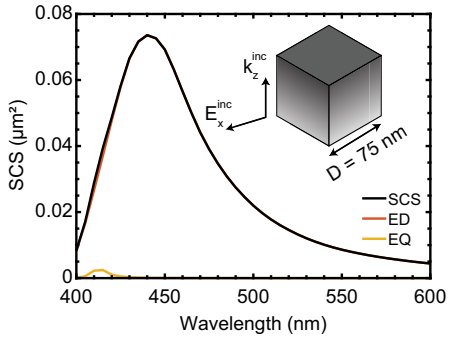

Fig. 15. Reference SCS for a silver cube ($D = 75$ nm).

25,746 DoF. In order to study the convergence, we discretize the nanoparticle's geometry with a triangular or a rectangular mesh that is refined up to approximately 20,000 DoF, as in Fig. 17.

First, we observe the accuracy at the resonance wavelength $\lambda = 440$ nm in Fig. 18(a) and the average relative error R_E over the whole spectrum in Fig. 18(b). The wavelength scanning step is 5 nm, so $\Lambda = 41$. The results show a better accuracy behavior of the rectangular mesh in both cases. The lower error factor R_E for the rectangular discretization stems mainly from its increased accuracy at shorter wavelengths, i.e., between 400 and 435 nm. Thus, with the use of hybrid meshes, except for the reduction of the number of unknowns and the size of the final system matrix, we could expect accuracy improvements, especially for geometries with rectangular or cylindrical surfaces that can be well approximated with these elements.

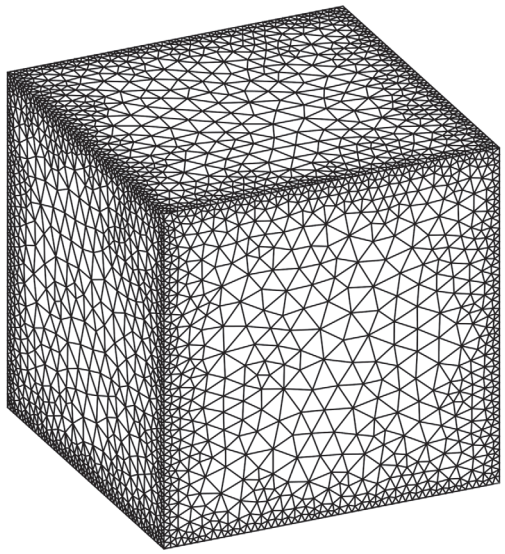

Fig. 16. Triangular mesh for the reference solution.

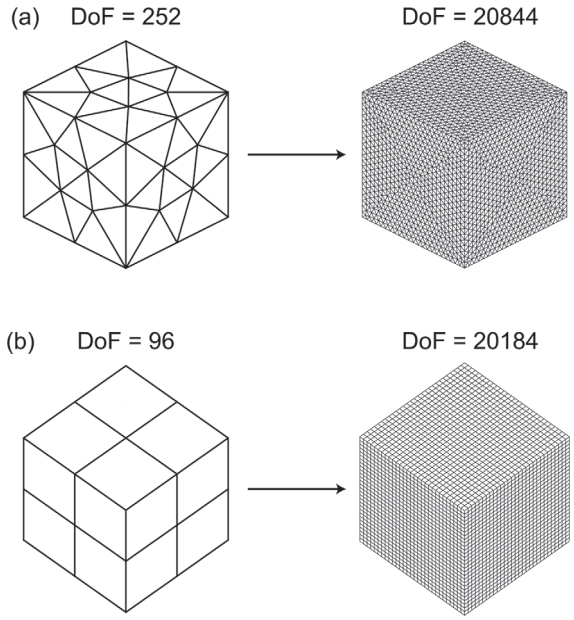

Fig. 17. Initial and final discretization refinement stages for the cube, using (a) a triangular mesh and (b) a rectangular mesh.

Another very important aspect of this comparison is the amount of time needed for the computation of the solution. In order to address it, we present in Fig. 19 the total simulation time for both mesh types as a function of DoF. The most time-consuming procedures are filling the final system matrix and solving the system with the direct method of LU factorization. For small numbers of DoF, the contribution of these procedures is similar (solving the linear system requires a little bit more time), whereas the time needed for filling the matrix of the final system dominates the total time as the DoF surpasses 5000. For the result in Fig. 19, all processes were implemented on a server with Intel Xeon Gold 6226R at 2.9 GHz as its central processing unit (CPU). In Fig. 19, a trade-off between accuracy and time can be observed since, for DoF > 5000, rectangular meshes require slightly more computational time than triangular meshes. However, this is not a detrimental indication against the utilization of hybrid meshes since the time difference is not significant and the hybrid discretization approach aims to employ rectangular elements only on parts of the surface geometry. Lastly, additional accuracy results for a silver cube with fabrication imperfections (round edges) and hybrid discretization are presented in Supplement 1.

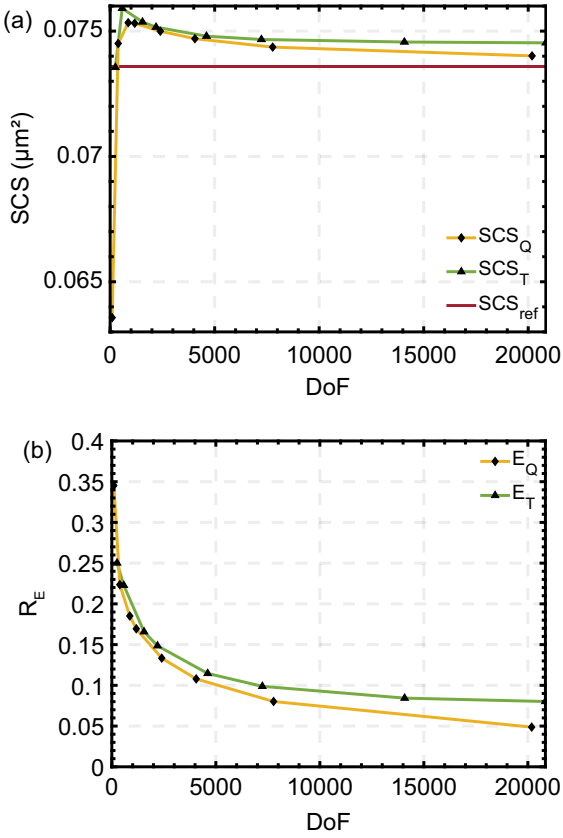

Fig. 18. Accuracy and convergence comparisons between triangular and quadrilateral meshes for a silver cube. (a) SCS accuracy at the resonance $\lambda = 440$ nm, and (b) convergence of the relative error over the whole spectrum.

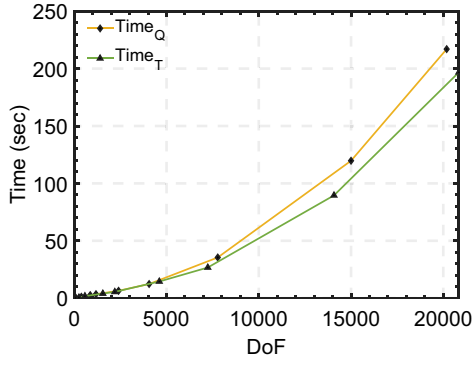

Fig. 19. Total simulation time at the resonance ($\lambda = 440$ nm).

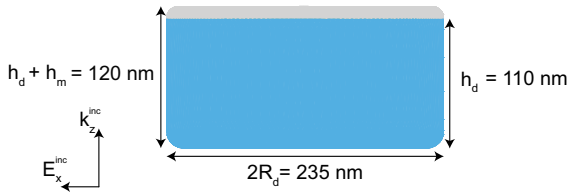

Fig. 20. Hybrid meta-atom geometry built from an aSi cylinder (light blue) capped with an Ag disk (light gray) in a water background.

C. Hybrid Meta-Atom

As a last example, we examine a hybrid meta-atom that consists of a silver disk (light gray) on top of an amorphous silicon cylinder (light blue) in a water background, as shown in Fig. 20. Such a structure that combines electric and magnetic responses at the nanoscale has a rich spectral response and is interesting to build metasurfaces [15,22,71,72]. In order to consider fabrication imperfections, the circular edges of the geometry are rounded (curvature radii are 10 nm and 15 nm for top and bottom edges, respectively).

In this section, we introduce the Green's function singularity subtraction technique as in Ref. [70], which removes the need to properly select integration points that avoid singularities. In order to apply this approach, the Green's function in a domain Ω_i has to be expanded in a Taylor series, where the odd terms are the singular ones. Subsequently, the Green's function can be divided into a smooth part (free of singularities) and a singular part [73], as $G_i(\mathbf{r}, \mathbf{r}') = G_i^s(\mathbf{r}, \mathbf{r}') + T_i(\mathbf{r}, \mathbf{r}')$, where the smooth part $G_i^s(\mathbf{r}, \mathbf{r}')$ can be numerically integrated and the singular part $T_i(\mathbf{r}, \mathbf{r}')$ can be integrated semi-analytically with the help of closed-form relations. The integrals that occur from the implementation of the singularity subtraction method are solved semi-analytically. The corresponding expressions for the cases of RWG, rooftop, and hybrid basis functions can be found in Ref. [70].

The reference SCS response is obtained with the triangular mesh (DOF = 35,158) depicted in Fig. 21(a). In order to test the accuracy of the hybrid discretization, we consider a coarser triangular mesh $\mathcal{T}$ and two hybrid meshes with different numbers of rectangular elements $\mathcal{H}_1$ and $\mathcal{H}_2$. All three aforementioned meshes only differ in the discretization of the cylindrical side surface, as can be observed in Figs. 21(b), 21(c), and 21(d). This way we are able to investigate how decreasing the DoF with hybrid meshes affects accuracy and simulation time. The numbers of DoF are mentioned in the respective legends in Fig. 21.

In Fig. 22, we provide the SCS results for the aforementioned discretizations of this hybrid nanostructure. Although there are some minor differences around $\lambda = 800$ nm, they do not change the overall SCS. Hence, there is an almost identical behavior in terms of accuracy. More significantly, hybrid meshes are able to accurately reproduce very narrow scattering features, e.g., the extremely sharp decrease of the SCS response at $\lambda = 970$ nm, even with a significantly reduced number of unknowns.

Another important aspect of this comparison is the required computational time. In Fig. 23, we present the total simulation time for the different meshes at the wavelength of the narrow SCS dip ($\lambda = 970$ nm). In the graph, t_{sol} stands for the linear system solution time with LU factorization, t_{fill} depicts the time

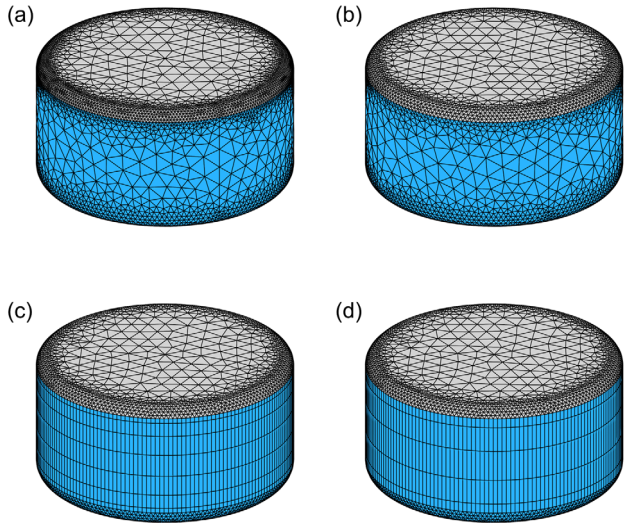

Fig. 21. Triangular and hybrid discretizations of the geometry shown in Fig. 20; (a) reference triangular mesh (DoF = 35158), (b) triangular mesh $\mathcal{T}$ (DoF = 27278), (c) hybrid mesh $\mathcal{H}_2$ (DoF = 26292), and (d) hybrid mesh $\mathcal{H}_1$ (DoF = 24820).

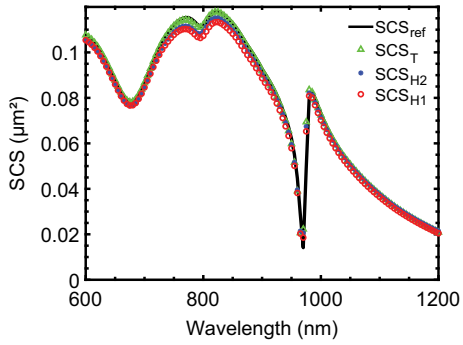

Fig. 22. SCS comparison between triangular and hybrid meshes.

needed for filling the final system matrix, and t_{rest} is the remaining seconds of the simulation. As expected, the hybrid meshes provide accurate solutions faster since the number of DoF is significantly reduced. Additionally, an interesting observation is that the time required to fill the final system matrix increases at a much higher rate with the DoF compared to the time needed for solving the final system, making it the primary contributor to the total computational time for large numbers of DoF. This outcome arises from the very large number of integration points employed for numerical integration within each mesh element, a choice made to ensure high accuracy in the simulation. While this effect is pronounced for the relatively small systems considered here, it is expected that for larger systems, the cubic scaling of LU decomposition will eventually dominate the computational cost, aligning with typical observations in SIE solvers.

The Green's function singularity subtraction technique allows the determination of the field distribution arbitrarily close to the boundaries of the different domains. For instance, by utilizing the hybrid mesh $\mathcal{H}_1$, one can compute and visualize the intensity distribution of the electric field $|\mathbf{E}|^2$ on the $y = 0$ plane that intersects the hybrid meta-atom structure,

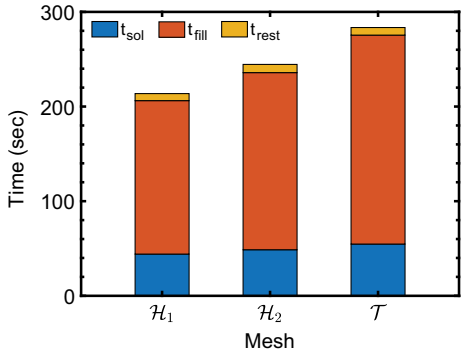

Fig. 23. Total simulation time comparison for the different meshes.

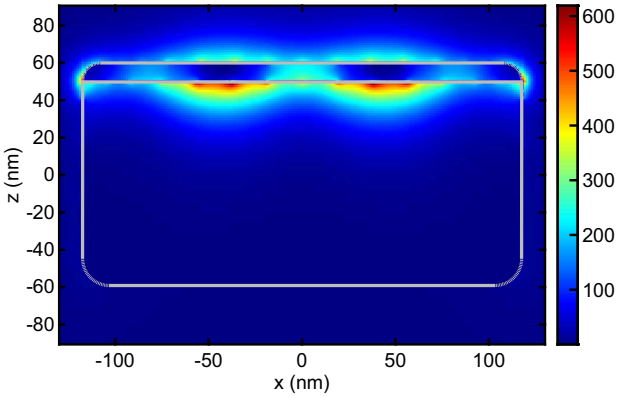

Fig. 24. Electric field intensity $|\mathbf{E}|^2$ around and inside the hybrid meta-atom, determined by using the hybrid discretization $\mathcal{H}_1$. The illumination intensity is $|\mathbf{E}^{\text{inc}}|^2 = 1$.

as shown in Fig. 24. The selected wavelength is $\lambda = 970$ nm, which corresponds to the minimum of the SCS response. It is obvious that most of the electric field is confined inside the aSi cylinder (below its interface with the Ag disk). The homogeneous triangular and hybrid discretizations provide near-field results with almost perfect agreement, even though the latter requires a smaller number of unknowns. Lastly, the near-field comparison between meshes $\mathcal{T} - \mathcal{H}_1$ and an additional study of the method's iterative convergence for $\mathcal{H}_1$, $\mathcal{H}_2$, and $\mathcal{T}$ are provided in Supplement 1.

5. CONCLUSION AND OUTLOOK

A hybrid mesh approach for modeling nanostructures was presented and investigated in this paper. The accuracy and computational time were discussed for different plasmonic and hybrid nanoparticles. From the theoretical analysis and the numerical implementation, it can be concluded that, for the examined scenarios, hybrid discretization techniques contribute to the significant decrease of the number of unknowns without accuracy penalties. Furthermore, the size of the final linear system is the main contribution to the computational time since solving the system requires much less time compared to filling the matrix. Finally, we would like to propose some possible directions for future research in hybrid discretization schemes for SIEs: the investigation of the performance of different formulations with hybrid meshes (e.g., mN-Müller or JMCFIE), the application of higher-order basis functions in both triangular and quadrilateral elements of hybrid meshes, the simultaneous utilization of curvilinear triangles and quadrilaterals, the implementation of different testing procedures, and the search for entire-domain basis functions that can reduce the total number of unknowns in SIE formulations as in Ref. [74].

Funding. Schweizerischer Nationalfonds zur Förderung der Wissenschaftlichen Forschung (under project 200021 212758).

Disclosures. The authors declare no conflicts of interest.

Data availability. Data underlying the results presented in this paper are not publicly available at this time but may be obtained from the authors upon reasonable request.

Supplemental document. See Supplement 1 for supporting content.

REFERENCES

1. J. Wang and J. Du, "Plasmonic and dielectric metasurfaces: design, fabrication and applications," Appl. Sci. **6**, 239 (2016).
2. F. Monticone and A. Alù, "Metamaterial, plasmonic and nanophotonic devices," Rep. Prog. Phys. **80**, 036401 (2017).
3. J. P. Kottmann, O. J. F. Martin, D. R. Smith, *et al.*, "Field polarization and polarization charge distributions in plasmon resonant nanoparticles," New J. Phys. **2**, 27 (2000).
4. Y. Ekinci, A. Christ, M. Agio, *et al.*, "Electric and magnetic resonances in arrays of coupled gold nanoparticle in-tandem pairs," Opt. Express **16**, 13287–13295 (2008).
5. Y. Yang, I. I. Kravchenko, D. P. Briggs, *et al.*, "All-dielectric metasurface analogue of electromagnetically induced transparency," Nat. Commun. **5**, 5753 (2014).
6. A. I. Kuznetsov, A. E. Miroshnichenko, M. L. Brongersma, *et al.*, "Optically resonant dielectric nanostructures," Science **354**, aag2472 (2016).
7. N. Bontempi, K. E. Chong, H. W. Orton, *et al.*, "Highly sensitive biosensors based on all-dielectric nanoresonators," Nanoscale **9**, 4972–4980 (2017).
8. D. Tzarouchis and A. Sihvola, "Light scattering by a dielectric sphere: perspectives on the Mie resonances," Appl. Sci. **8**, 184 (2018).
9. K. Koshelev and Y. Kivshar, "Dielectric resonant metaphotonics," ACS Photonics **8**, 102–112 (2021).
10. K. Achouri, A. Kiselev, and O. J. F. Martin, "Multipolar origin of electromagnetic transverse force resulting from two-wave interference," Phys. Rev. B **102**, 085107 (2020).
11. A. Kiselev, K. Achouri, and O. J. F. Martin, "Multipole interplay controls optical forces and ultra-directional scattering," Opt. Express **28**, 27547–27560 (2020).
12. M. F. Limonov, M. V. Rybin, A. N. Poddubny, *et al.*, "Fano resonances in photonics," Nat. Photonics **11**, 543–554 (2017).
13. D. Darvill, A. Centeno, and F. Xie, "Plasmonic fluorescence enhancement by metal nanostructures: shaping the future of bionanotechnology," Phys. Chem. Chem. Phys. **15**, 15709–15726 (2013).
14. X. Han, K. Liu, and C. Sun, "Plasmonics for biosensing," Materials (Basel) **12**, 1411 (2019).
15. D. Ray, A. Kiselev, and O. J. F. Martin, "Multipolar scattering analysis of hybrid metal-dielectric nanostructures," Opt. Express **29**, 24056–24067 (2021).
16. S. S. Kruk, L. Wang, B. Sain, *et al.*, "Asymmetric parametric generation of images with nonlinear dielectric metasurfaces," Nat. Photonics **16**, 561–565 (2022).
17. A. Devilez, B. Stout, and N. Bonod, "Compact metallo-dielectric optical antenna for ultra directional and enhanced radiative emission," ACS Nano **4**, 3390–3396 (2010).
18. X. Zeng, W. Yu, P. Yao, *et al.*, "Metallo-dielectric hybrid antenna for high Purcell factor and radiation efficiency," Opt. Express **22**, 14517–14523 (2014).
19. S. Sun, T. Zhang, Q. Liu, *et al.*, "Enhanced directional fluorescence emission of randomly oriented emitters via a metal–dielectric hybrid nanoantenna," J. Phys. Chem. C **123**, 21150–21160 (2019).

20. S. Sun, M. Li, Q. Du, *et al.*, "Metal–dielectric hybrid dimer nanoantenna: coupling between surface plasmons and dielectric resonances for fluorescence enhancement," J. Phys. Chem. C **121**, 12871–12884 (2017).
21. S. Sun, R. Li, M. Li, *et al.*, "Hybrid mushroom nanoantenna for fluorescence enhancement by matching the Stokes shift of the emitter," J. Phys. Chem. C **122**, 14771–14780 (2018).
22. D. Ray, T. V. Raziman, C. Santschi, *et al.*, "Hybrid metal-dielectric metasurfaces for refractive index sensing," Nano Lett. **20**, 8752–8759 (2020).
23. A. Kiselev, D. Ray, and O. J. F. Martin, "Multipolar scattering analysis of a hybrid metal-dielectric stacked nanoantenna," in *Plasmonics: Design, Materials, Fabrication, Characterization, and Applications XIX*, Y.-J. Lu, T. Tanaka, and D. P. Tsai, eds. (SPIE, 2021).
24. B. M. Kolundzija, "Electromagnetic modeling of composite metallic and dielectric structures," IEEE Trans. Microw. Theory Tech. **47**, 1021–1032 (1999).
25. U. Hohenester, *Nano and Quantum Optics*, 1st ed. (Springer Nature, 2019).
26. U. Hohenester and G. Unger, "Nanoscale electromagnetism with the boundary element method," Phys. Rev. B **105**, 075428 (2022).
27. U. Hohenester, N. Reichelt, and G. Unger, "Nanophotonic resonance modes with the nanobem toolbox," Comput. Phys. Commun. **276**, 108337 (2022).
28. B. Gallinet, J. Butet, and O. J. F. Martin, "Numerical methods for nanophotonics: standard problems and future challenges," Laser Photonics Rev. **9**, 577–603 (2015).
29. I. Fredholm, "Sur une classe d'équations fonctionnelles," Acta Math. **27**, 365–390 (1903).
30. P. Ylä-Oijala, S. P. Kiminki, J. Markkanen, *et al.*, "Error-controllable and well-conditioned MoM solutions in computational electromagnetics: ultimate surface integral-equation formulation," IEEE Antennas Propag. Mag. **55**, 310–331 (2013).
31. A. J. Poggio and E. K. Miller, "Integral equation solutions of three-dimensional scattering problems," in *Computer Techniques for Electromagnetics* (Elsevier, 1973), pp. 159–264.
32. T.-K. Wu and L. L. Tsai, "Scattering from arbitrarily-shaped lossy dielectric bodies of revolution," Radio Sci. **12**, 709–718 (1977).
33. Y. Chang and R. Harrington, "A surface formulation for characteristic modes of material bodies," IRE Trans. Antennas Propag. **25**, 789–795 (1977).
34. S. Yan, J.-M. Jin, and Z. Nie, "Improving the accuracy of the second-kind Fredholm integral equations by using the Buffa-Christiansen functions," IEEE Trans. Antennas Propag. **59**, 1299–1310 (2011).
35. C. Forestiere, G. Iadarola, G. Rubinacci, *et al.*, "Surface integral formulations for the design of plasmonic nanostructures," J. Opt. Soc. Am. A **29**, 2314–2327 (2012).
36. P. Ylä-Oijala, J. Markkanen, S. Jarvenpaa, *et al.*, "Surface and volume integral equation methods for time-harmonic solutions of Maxwell's equations," Prog. Electromagn. Res. **149**, 15–44 (2014).
37. M. G. Araújo, J. M. Taboada, D. M. Solís, *et al.*, "Comparison of surface integral equation formulations for electromagnetic analysis of plasmonic nanoscatterers," Opt. Express **20**, 9161–9171 (2012).
38. P. Ylä-Oijala, M. Taskinen, and S. Järvenpää, "Surface integral equation formulations for solving electromagnetic scattering problems with iterative methods," Radio Sci. **40**, 1–19 (2005).
39. D. M. Sols, J. M. Taboada, O. Rubiños-López, *et al.*, "Improved combined tangential formulation for electromagnetic analysis of penetrable bodies," J. Opt. Soc. Am. B **32**, 1780–1787 (2015).
40. P. Ylä-Oijala and M. Taskinen, "Application of combined field integral equation for electromagnetic scattering by dielectric and composite objects," IEEE Trans. Antennas Propag. **53**, 1168–1173 (2005).
41. E. Jorgensen, J. L. Volakis, P. Meincke, *et al.*, "Higher order hierarchical Legendre basis functions for electromagnetic modeling," IEEE Trans. Antennas Propag. **52**, 2985–2995 (2004).
42. B. M. Notaros, "Higher order frequency-domain computational electromagnetics," IEEE Trans. Antennas Propag. **56**, 2251–2276 (2008).
43. B. C. Usner, K. Sertel, M. A. Carr, *et al.*, "Generalized volume-surface integral equation for modeling inhomogeneities within high contrast composite structures," IEEE Trans. Antennas Propag. **54**, 68–75 (2006).
44. M. Djordjevic and B. M. Notaros, "Double higher order method of moments for surface integral equation modeling of metallic and dielectric antennas and scatterers," IEEE Trans. Antennas Propag. **52**, 2118–2129 (2004).
45. P. Ylä-Oijala, S. P. Kiminki, K. Cools, *et al.*, "Mixed discretization schemes for electromagnetic surface integral equations," Int. J. Numer. Model. **25**, 525–540 (2012).
46. E. Ubeda and J. M. Rius, "Novel monopolar MFIE MoM-discretization for the scattering analysis of small objects," IEEE Trans. Antennas Propag. **54**, 50–57 (2006).
47. L. Zhang, A. Deng, M. Wang, *et al.*, "Numerical study of a novel MFIE formulation using monopolar RWG basis functions," Comput. Phys. Commun. **181**, 52–60 (2010).
48. P. Ylä-Oijala, M. Taskinen, and S. Järvenpää, "Analysis of surface integral equations in electromagnetic scattering and radiation problems," Eng. Anal. Bound. Elem. **32**, 196–209 (2008).
49. X. Wan, Y. Liu, and C. Wu, "The research of magnetic-field integration method based on linear-linear basis functions," Procedia Comput. Sci. **183**, 783–790 (2021).
50. W. Cai, T. Yu, H. Wang, *et al.*, "High-order mixed RWG basis functions for electromagnetic applications," IEEE Trans. Microw. Theory Tech. **49**, 1295–1303 (2001).
51. R. Chang and V. Lomakin, "Quadrilateral barycentric basis functions for surface integral equations," IEEE Trans. Antennas Propag. **61**, 6039–6050 (2013).
52. T. F. Eibert, J. L. Volakis, D. R. Wilton, *et al.*, "Hybrid FE/BI modeling of 3-D doubly periodic structures utilizing triangular prismatic elements and an MPIE formulation accelerated by the Ewald transformation," IEEE Trans. Antennas Propag. **47**, 843–850 (1999).
53. Y. Ren, Y. Chen, Q. Zhan, *et al.*, "A higher order hybrid SIE/FEM/SEM method for the flexible electromagnetic simulation in layered medium," IEEE Trans. Geosci. Remote Sens. **55**, 2563–2574 (2017).
54. Z. Zeng and C.-C. Lu, "Discretization of hybrid VSIE using mixed mesh elements with zeroth-order Galerkin basis functions," IEEE Trans. Antennas Propag. **54**, 1863–1870 (2006).
55. A. M. Kern and O. J. F. Martin, "Surface integral formulation for 3D simulations of plasmonic and high permittivity nanostructures," J. Opt. Soc. Am. A **26**, 732–740 (2009).
56. S. Rao, D. Wilton, and A. Glisson, "Electromagnetic scattering by surfaces of arbitrary shape," IEEE Trans. Antennas Propag. **30**, 409–418 (1982).
57. J. L. Volakis and K. Sertel, *Integral Equation Methods for Electromagnetics* (SciTech Publishing, 2012).
58. O. J. F. Martin and N. B. Piller, "Electromagnetic scattering in polarizable backgrounds," Phys. Rev. E **58**, 3909–3915 (1998).
59. P. Ylä-Oijala, M. Taskinen, and J. Sarvas, "Surface integral equation method for general composite metallic and dielectric structures with junctions," Prog. Electromagn. Res. **52**, 81–108 (2005).
60. R. F. Harrington, "Two-dimensional electromagnetic fields," in *Field Computation by Moment Methods* (Wiley-IEEE Press, 1993), pp. 41–61.
61. R. F. Harrington, "Boundary integral formulations for homogeneous material bodies," J. Electromagn. Waves Appl. **3**, 1–15 (1989).
62. A. F. Peterson, "Divergence-conforming basis functions," in *Mapped Vector Basis Functions for Electromagnetic Integral Equations* (Springer International Publishing, 2006), pp. 25–51.
63. A. F. Peterson, "Curl-conforming basis functions," in *Mapped Vector Basis Functions for Electromagnetic Integral Equations* (Springer International Publishing, 2006), pp. 53–69.
64. B. M. Notaros, B. D. Popovic, J. P. Weem, *et al.*, "Efficient large-domain MoM solutions to electrically large practical EM problems," IEEE Trans. Microw. Theory Tech. **49**, 151–159 (2001).
65. G. E. Antilla and N. G. Alexopoulos, "Scattering from complex three-dimensional geometries by a curvilinear hybrid finite-element–integral equation approach," J. Opt. Soc. Am. A **11**, 1445–1457 (1994).
66. C. F. Bohren and D. R. Huffman, *Absorption and Scattering of Light by Small Particles* (John Wiley & Sons, 1998).
67. T. V. Raziman, W. R. C. Somerville, O. J. F. Martin, *et al.*, "Accuracy of surface integral equation matrix elements in plasmonic calculations," J. Opt. Soc. Am. B **32**, 485–492 (2015).

68. D. Ray, A. Kiselev, and O. J. F. Martin, "Refractive index data for 150 nm Ag measured with ellipsometry," Zenodo (2021), https://zenodo.org/records/4552069.
69. D. T. Pierce and W. E. Spicer, "Electronic structure of amorphous Si from photoemission and optical studies," Phys. Rev. **5**, 3017–3029 (1972).
70. I. Hanninen, M. Taskinen, and J. Sarvas, "Singularity subtraction integral formulae for surface integral equations with RWG, rooftop and hybrid basis functions," Prog. Electromagn. Res. **63**, 243–278 (2006).
71. E. Rusak, I. Staude, M. Decker, *et al.*, "Hybrid nanoantennas for directional emission enhancement," Appl. Phys. Lett. **105**, 221109 (2014).
72. R. Guo, E. Rusak, I. Staude, *et al.*, "Multipolar coupling in hybrid metal–dielectric metasurfaces," ACS Photonics **3**, 349–353 (2016).
73. J. P. Kottmann and O. J. F. Martin, "Accurate solution of the volume integral equation for high-permittivity scatterers," IEEE Trans. Antennas Propag. **48**, 1719–1726 (2000).
74. C. Forestiere, G. Gravina, G. Miano, *et al.*, "Static surface mode expansion for the electromagnetic scattering from penetrable objects," IEEE Trans. Antennas Propag. **71**, 6779–6793 (2023).